Modulation of *Tmem135* Leads to Retinal Pigmented Epithelium Pathologies in Mice

Michael Landowski,[1–3] Samuel Grindel,[1] Pawan K. Shahi,[2,3] Abigail Johnson,[1] Daniel Western,[1] Adrienne Race,[1] Franky Shi,[1] Jonathan Benson,[1] Marvin Gao,[1] Evelyn Santoirre,[1] Wei-Hua Lee,[1] Sakae Ikeda,[1,2] Bikash R. Pattnaik,[2,3] and Akihiro Ikeda[1,2]

[1]Department of Medical Genetics, University of Wisconsin-Madison, Madison, Wisconsin, United States
[2]McPherson Eye Research Institute, University of Wisconsin-Madison, Madison, Wisconsin, United States
[3]Department of Pediatrics, Ophthalmology and Visual Sciences, University of Wisconsin-Madison, Madison, Wisconsin, United States

Correspondence: Akihiro Ikeda, Department of Medical Genetics, University of Wisconsin-Madison, Room 5350 Genetics-Biotech, 425-G Henry Mall, Madison, 53706 WI, USA;
aikeda@wisc.edu.

Received: May 26, 2020
Accepted: September 23, 2020
Published: October 16, 2020

Citation: Landowski M, Grindel S, Shahi PK, et al. Modulation of *Tmem135* leads to retinal pigmented epithelium pathologies in mice. *Invest Ophthalmol Vis Sci.* 2020;61(12):16.
https://doi.org/10.1167/iovs.61.12.16

Purpose. Aging is a critical risk factor for the development of retinal diseases, but how aging perturbs ocular homeostasis and contributes to disease is unknown. We identified transmembrane protein 135 (*Tmem135*) as a gene important for regulating retinal aging and mitochondrial dynamics in mice. Overexpression of *Tmem135* causes mitochondrial fragmentation and pathologies in the hearts of mice. In this study, we examine the eyes of mice overexpressing wild-type *Tmem135* (*Tmem135* TG) and compare their phenotype to *Tmem135* mutant mice.

Methods. Eyes were collected for histology, immunohistochemistry, electron microscopy, quantitative PCR, and Western blot analysis. Before tissue collection, electroretinography (ERG) was performed to assess visual function. Mouse retinal pigmented epithelium (RPE) cultures were established to visualize mitochondria.

Results. Pathologies were observed only in the RPE of *Tmem135* TG mice, including degeneration, migratory cells, vacuolization, dysmorphogenesis, cell enlargement, and basal laminar deposit formation despite similar augmented levels of *Tmem135* in the eyecup (RPE/choroid/sclera) and neural retina. We observed reduced mitochondria number and size in the *Tmem135* TG RPE. ERG amplitudes were decreased in 365-day-old mice overexpressing *Tmem135* that correlated with reduced expression of RPE cell markers. In *Tmem135* mutant mice, RPE cells are thicker, smaller, and denser than their littermate controls without any signs of degeneration.

Conclusions. Overexpression and mutation of *Tmem135* cause contrasting RPE abnormalities in mice that correlate with changes in mitochondrial shape and size (overfragmented in TG vs. overfused in mutant). We conclude proper regulation of mitochondrial homeostasis by TMEM135 is critical for RPE health.

Keywords: RPE, aging, mitochondria

Aging imposes significant stress on the retina and contributes to the development of age-related macular degeneration (AMD),[1] diabetic retinopathy,[2] and glaucoma.[3] Although there is an excellent understanding of the pathways disturbed by aging,[4] it is unclear how aging influences the risk for these debilitating age-dependent retinal diseases. Studying how aging perturbs retinal homeostasis may lead to novel therapies for age-dependent retinal diseases because the prevalence of such diseases are expected to increase in the future dramatically.[5–7]

To identify critical pathways involved in retinal aging, we used forward genetics to uncover genes harboring mutations responsible for accelerated aging retinal phenotypes in mice. Using this approach, we studied an ENU-induced mutant mouse line, *FUN025*, displaying visual loss, photoreceptor degeneration, thicker retinal pigmented epithelium (RPE), increased ectopic synapses, and neuroinflammation.[8] Positional cloning of *FUN025* revealed a mutation in transmembrane protein 135 (*Tmem135*) as causal for the accelerated aging retinal phenotype in the *FUN025* line.[8] *Tmem135* encodes a 52 kilodalton protein with five transmembrane domains that share similarities with the Tim17 protein family, a group of proteins important for mitochondria biogenesis.[8,9] TMEM135 can localize with mitochondria,[8] as well as peroxisomes,[10,11] and lipid droplets.[10] The molecular function of TMEM135 is unclear but has a role in regulating mitochondrial dynamics.[8] "Mitochondrial dynamics" is the collective term for the fusion, fission, and mitophagy events mitochondria undergo to preserve their shape, number, and function.[12] Primary-cultured murine fibroblasts expressing mutant TMEM135 and overexpressing wild-type (WT) TMEM135 show increased numbers of elongated and fragmented mitochondria, respectively.[8] Elucidating the function of TMEM135 on mitochondrial dynamics in the

murine eye may shed insight into how aging affects retinal homeostasis.

Tmem135 overexpression leads to excess cardiac mitochondrial fission and pathologies, including hypertrophy, fibrosis, and collagen accumulation in mice.[13] It is unknown whether *Tmem135* overexpression affects the eye. In this study, we evaluated the eyes of mice overexpressing WT *Tmem135* (*Tmem135* TG) for pathologies and compared our findings to those in *Tmem135*$^{FUN025/FUN025}$ mutant mice.

Materials and Methods

Animals

All experiments performed in this study were in accordance with the National Institutes of Health (NIH) Guide for the Care and Use of Laboratory Animals and were authorized by the Animal Care and Use Committee at the University of Wisconsin-Madison. Generation of *Tmem135* TG and *Tmem135*$^{FUN025/FUN025}$ mice was previously described.[8,13] For the current study, we generated *Tmem135* TG mice congenic on the C57BL/6J background by crossing *Tmem135* TG mice on the mixed background with C57BL/6J mice for at least 10 generations. None of the mice used in this study carried either the *Ped6b*^{rd1} or the *Crb1*^{rd8} mutation.[14,15] Age-matched littermate WT mice served as controls for *Tmem135* TG mice, and *Tmem135*$^{FUN025/+}$ littermates were used as controls for *Tmem135*$^{FUN025/FUN025}$ mice. Both female and male mice were used in this study, but no gender differences were observed, and figures include data from both genders. All ages, genders, and cohorts of WT and *Tmem135* TG, as well as *Tmem135*$^{FUN025/+}$ and *Tmem135*$^{FUN025/FUN025}$ mice, are summarized in Supplementary Tables S1 and S2, respectively. All numbers and ages of mice used for experiments are also listed in the figure legends. All animals were treated in accordance with the ARVO Statement for the Use of Animals in Ophthalmic and Vision Research.

RNA Isolation, cDNA Preparation, and Quantitative PCR

Tissues were collected from the mice and kept at –80°C degrees. RNA was extracted using an RNeasy lipid tissue mini kit (#74804; Qiagen, Germantown, MD, USA) according to the manufacturer's instructions. RNA concentrations were determined using the Nanodrop 2000 UV-Vis Spectrophotometer (Thermo Fisher Scientific, Waltham, MA, USA). Equal RNA concentrations were used to make cDNA using an Oligo d(T)18 primer (#S1316S; NEB, Ipswich, MA, USA) and the ProtoScript II Reverse Transcriptase (#M0368L; NEB) following the manufacturer's protocol. Expression of each gene was assessed in triplicate reactions in the Roche Lightcycler 480 system using cDNA, 200 nmol/L of each primer, and Lightcycler 480 SYBR Green I Supermix (#507203180; Roche, Indianapolis, IN, USA). Primer sequences used in this study are described in Supplementary Table S3. Relative mRNA expression was normalized to the ribosomal protein lateral stalk subunit P0 (Rlpl0) using the quantitative $2^{-\Delta\Delta CT}$ method.[16]

Histology

Eyes were fixed in 2% paraformaldehyde (PFA) and 2% glutaraldehyde solution overnight at 4°C and submitted to the University of Wisconsin-Madison's Translational Research Initiatives in Pathology (TRIP) core for paraffin embedding, processing, and sectioning. Sections were stained with hematoxylin and eosin to visualize retinal architecture and imaged using an Axio Imager 2 microscope (Carl Zeiss MicroImaging, White Plains, NY, USA) at a 40X magnification. Images were analyzed using ImageJ software (NIH, Bethesda, MD, USA). The thickness of the RPE, outer nuclear layer (ONL), and inner nuclear layer (INL) were measured on a single section from each eye that had a visible optic nerve head. Measurements were started from the optic nerve head and taken at seven consecutive 300-µm intervals. Quantification of RPE pathologies (i.e., migratory cells and vacuolization) were assessed on six retinal sections that were separated by 50 µm. The total number of RPE pathologies were divided by the total number of slides to generate the frequency of RPE pathologies per eye.

Immunohistochemistry

Eyes were fixed in 4% PFA overnight at 4°C, processed for cryoprotection and embedded in Tissue-Tek O.C.T. Compound (Sakura Finetek USA, Torrance, CA, USA). Sections were cut at 10-µm thickness on a cryostat. We labeled subretinal immune cells with rabbit anti-ionized calcium binding adaptor molecule 1 (IBA-1) (# 019–19741; Wako, Richmond, VA) as previously described.[8,17] One retinal section per mouse was imaged using a Nikon A1RS confocal microscope (Nikon, Tokyo, Japan) at a 40X magnification, and IBA-1 positive immune cells between the RPE and ONL were counted using ImageJ software (NIH).

RPE Flat Mounts

Eyes were enucleated and dissected to remove the anterior segment, lens, and retina. The remaining posterior eyecup was fixed in methanol overnight and then washed with 1X PBS the next day. The eyecup was incubated with 10% normal donkey serum (#017-000-121; Jackson ImmunoResearch, West Grove, PA, USA) for at least 30 minutes and then switched to a 1:50 dilution of a rabbit polyclonal zonula occludens-1 antibody (#40-2200; Thermo Fisher Scientific) overnight at 4°C. Then, the eyecups were rinsed with 1X PBS and incubated with a 1:250 dilution of an Alexa Fluor 488 conjugated donkey anti-rabbit IgG (#A-21206; Thermo Fisher Scientific) and 4′,6-Diamidine-2′-phenylindole dihydrochloride (DAPI) (#D9542; Sigma Aldrich, St. Louis, MO, USA) for 2 hours. The eyecups had a final rinse with 1X PBS and were mounted on slides. The RPE flat mounts were imaged with a Nikon A1RS confocal microscope at a 20X magnification. For each RPE flat mount, an image was obtained from the north, east, south, and west quadrants surrounding the optic nerve. RPE flat mounts were analyzed to determine RPE cell size and density. RPE cell size was calculated using the RPE Cell Profiler program (Broad Institute, Boston, MA, USA) that was previously used to measure RPE cell size in human donor eyes.[18] RPE cell density was assessed by counting the number of RPE cells using the Cell Counter Plugin in NIH's ImageJ program and dividing the number of total counted RPE cells by the total image area.

Electron Microscopy (EM)

Eyes were fixed with 2% PFA and 2% glutaraldehyde and submitted to the Electron Microscope Core at the University of Wisconsin-Madison for transmission EM processing

Investigative Ophthalmology & Visual Science

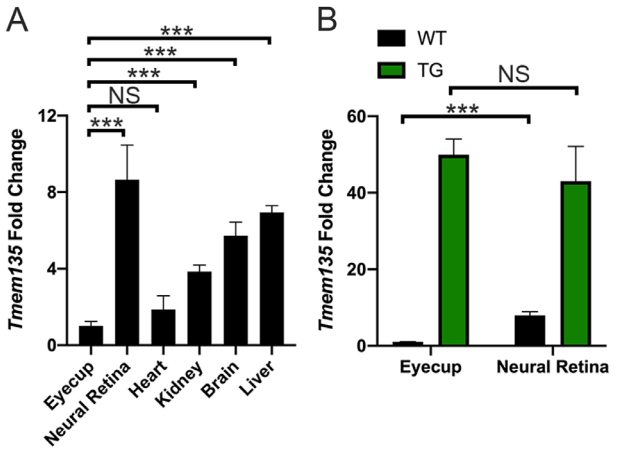

Figure 1. *Tmem135* expression in WT and *Tmem135* TG tissues. (**A**) Tissues were harvested from three 180-day-old WT mice for RNA isolation and quantitative PCR to assess *Tmem135* expression. Data were normalized to the eyecup (RPE/choroid/sclera) value. *Tmem135* is highly expressed in the neural retina compared with the eyecup and heart. (**B**) The eyecups and neural retinas were collected from four 30-day-old WT and *Tmem135* TG mice to confirm the *Tmem135* overexpression driven by the chicken *beta-actin* promoter. Both the eyecups and neural retinas of *Tmem135* TG mice had amplified *Tmem135* expression that were not different. Data were normalized to the WT eyecup value. ***$P < 0.001$, ANOVA. NS, not significant. All data are mean ± SD.

as previously described.[13] Eye sections were mounted on a 400-mesh thin bar grid and images were collected where the grid bars intersected the RPE using a Phillips CM120 STEM microscope (FEI Company, Hillsboro, OR, USA) at a 15,000X magnification. For this study, we collected 163 EM images for WT RPE and 99 images for *Tmem135* TG RPE. Mitochondria number, surface area, pigment granule number, Bruch's membrane (BrM) thickness, and basal laminar deposit frequency were determined using NIH's ImageJ software.

Electroretinography (ERG)

Prior to the ERG recording, mice were dark-adapted overnight. They were anesthetized with a cocktail of ketamine (80 mg/kg) and xylazine (16 mg/kg) diluted in PBS by subcutaneous injection under dim red light. The pupils were dilated with 1% tropicamide and placed on a heating pad set to 37°C to maintain body temperature and later placed on a temperature-regulated heating plate equipped with the system during the ERG recording.

A drop of sterile 2.5% hypromellose ophthalmic solution (Goniovisc; HUB Pharmaceuticals LLC, Rancho Cucamonga, CA) was applied to the cornea of the dilated eyes to prevent dehydration for the electrical contact and placement of the recording electrode. Needle electrodes were inserted through the nostril and on the back as reference and ground electrode, respectively. ERGs were recorded using the Espion system (Diagnosys LLC, Lowell, MA, USA). Scotopic recordings were obtained from dark-adapted animals, and the eyes were exposed to a sequential increment of flash intensities (0.1–30 cd.s/m^2) for 300 ms with a 2 second interval between the flashes. For the acquisition of c-wave, the eyes were flashed with light intensities of 2.5 and 25 cd.s/m^2 for 4 seconds. Photopic recordings were performed after the light adaptation of mice at 30 cd.m^2 background and also during the photopic recordings. The flash intensities used for the photopic recordings were 0.78, 1, 2.25, 5, and 10 cd.s/m^2. Only the 10 cd.s/m^2 recordings were used in this study. ERG components were measured using the Espion software (Diagnosys LLC) and analyzed using Origin2020 (OriginLab Corp., Northampton, MA, USA).

Western Blot Analysis

Neural retina, eyecup (RPE/choroid/sclera), and heart were isolated from mice and stored at –80°C. Neural retina, eyecup, and heart lysates were made with a tissue homogenizer in 100, 80, and 1000 µL of RIPA buffer (#P189901; Thermo Fisher Scientific) containing protease inhibitors (#11836170001; Thermo Fisher Scientific), respectively. Protein concentrations were quantified using a BCA Protein Assay Kit (#P123228; Thermo Fisher Scientific). Equal protein amounts were aliquoted and loaded onto 10% Bis-Tris Criterion XT gels (#3450112; Biorad, Hercules, CA, USA) in MOPS buffer (#1610788; Biorad) and transferred to nitrocellulose membranes (#102673-324; Biorad). A total of 20 µg of each eyecup lysate, 30 µg of each neural retina lysate, and 30 µg of each heart lysate was used for Western blot analysis in this study. Membranes were blocked with milk and probed overnight with their respective primary antibody at 4°C. The primary antibodies used in this study were anti-CRALBP (#ab15051; Abcam, Cambridge, MA, USA), anti-Rhodopsin (#ab5417; Abcam), and total rodent OXPHOS Western blot antibody cocktail, not total rodent OXPHOS whole-blood antibody cocktail (#ab110413; Abcam). For loading controls, blots containing neural retinal samples were reprobed for tubulin (#3873S; Cell Signaling Technologies, Danvers, MA), blots containing eyecup lysates were probed for succinate dehydrogenase A (SDHA) (#11998S; Cell Signaling Technologies) or beta-actin (ACTB) (#4970S; Cell Signaling Technologies), and blots containing heart lysates were probed for glyceraldehyde 3-phosphate dehydrogenase (GAPDH) (#MCA-1D4; EnCor Biotechnology, Gainesville, FL, USA). Blots were washed with TBST buffer and incubated with their corresponding secondary antibody. Secondary antibodies used in this study were either donkey antimouse or antirabbit and were obtained from LI-COR Biosciences (Lincoln, NE, USA). Blots were washed again with TBST and imaged using the Odyssey Imaging System (LI-COR Biosciences) and analyzed using NIH's ImageJ software. All immunobands were normalized to the loading control on the immunoblot.

RPE Cell Culture and Mitochondria Staining

The primary RPE cultures were carried out using a previously described method with a slight modification.[19,20] Specifically, RPE cells were continued to be cultured in T75 flasks in complete Dulbecco's modified Eagle's medium after the initial harvest and subcultured at a 1:3 dilution every 3 days until they were used at passage 5 and reached at least 80% confluence for the mitochondrial morphological analysis. We immunolabeled a subset of our cultures with antibodies against beta-catenin (#C2206; Sigma Aldrich) to image tight junctions and RPE65 (#ab13826; Abcam), OTX1/OTX2 (#ab21990; Abcam), and CRALBP (#ab15051; Abcam) as RPE markers. RPE cells were stained with MitoTracker Red CMXRos (#M7512; Thermo Fisher Scientific) and DAPI using the same protocol as previously described.[8]

Investigative Ophthalmology & Visual Science

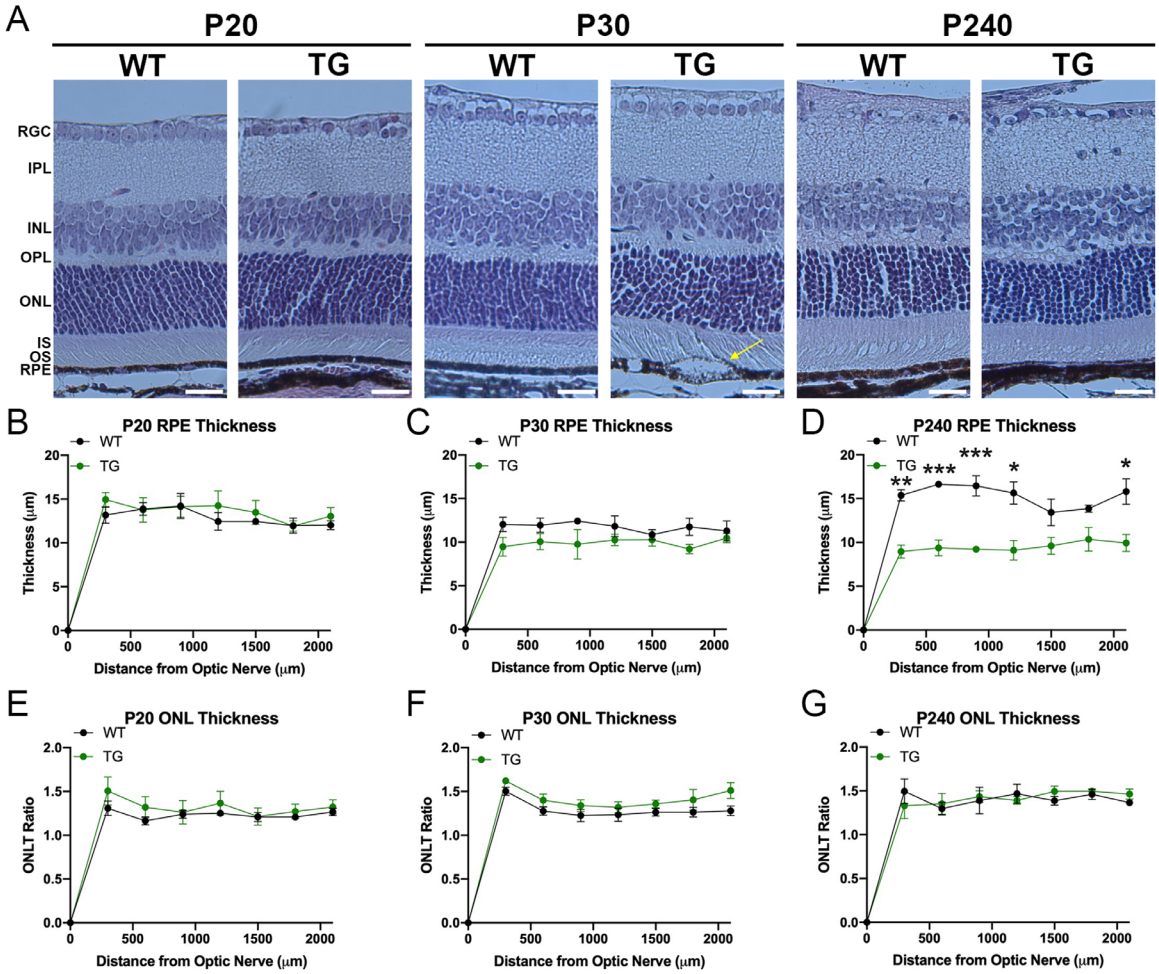

Figure 2. Retinal architecture in WT and *Tmem135* TG mice. (**A**) Representative images of the retina from P20, P30, and P240 WT and *Tmem135* TG mice. Note the large vacuolization (*yellow arrow*) in P30 *Tmem135* TG mice and thin RPE in P240 *Tmem135* TG mice. Magnification = 40X. *Scale bar* = 50 μm. (**B–D**) RPE thickness. There was a significant decrease in RPE thickness in P240 *Tmem135* TG mice. (**E–G**) ONLT ratios. There were no changes in ONLT ratios. Data from $n = 6$ WT (P20), $n = 4$ *Tmem135* TG (P20), $n = 5$ WT (P30), $n = 4$ *Tmem135* TG (P30), $n = 3$ WT (P240), and $n = 5$ *Tmem135* TG (P240). $^{*}P < 0.05$, $^{**}P < 0.01$, and $^{***}P < 0.001$, ANOVA. All data are mean ± SEM. RGC, retinal ganglion cell layer; IPL, inner plexiform layer; OPL, outer plexiform layer; IS, inner segments; OS, outer segments.

Statistics

GraphPad Prism software (GraphPad, San Diego, CA, USA) was used to perform analysis of variance (ANOVA) tests between tissues, genotypes at each age point, and *Tmem135* TG mice across ages in this study. Significance and error bar information is presented in each figure legend.

Results

Tmem135 Expression in Mouse Eye

Tmem135 is produced in the eyes and hearts of mice,[8,13] but the relative expression of *Tmem135* across various tissues in mice is not known. Multiple tissues, including eyecup, neural retina, heart, kidney, brain, and liver from WT C57BL/6J mice, were collected to evaluate *Tmem135* expression. The fold change of *Tmem135* expression relative to eyecup was 8.66 ± 1.82 in neural retina; 1.86 ± 0.72 in heart; 3.84 ± 0.35 in kidney; 5.72 ± 0.71 in brain; and 6.93 ± 0.36 in liver (Fig. 1A). These results suggest similar levels of *Tmem135* expression in the eyecups and hearts, which are lower than the neural retinas and other tissues of WT mice.

We also examined *Tmem135* levels in the neural retinas and eyecups of WT and *Tmem135* TG mice to confirm *Tmem135* overexpression. There was a dramatic augmentation in *Tmem135* expression in the eyecup (49.91 ± 4.12) and neural retina (43.05 ± 9.06) of *Tmem135* TG mice compared with the WT mice (Fig. 1B). The increased *Tmem135* expression was not statistically different between the eyecup and neural retina ($P = 0.22$). These data show comparable *Tmem135* overexpression in posterior eye tissues of *Tmem135* TG mice.

Histological Examination of *Tmem135* TG eyes

To determine if there is an effect of *Tmem135* overexpression on the retina, we collected eyes from 20-, 30-, and 240-day-old *Tmem135* TG mice for histology and compared them to age-matched WT littermates. At 20 days of age, we observed no differences between the retina of WT and *Tmem135* TG mice (Fig. 2A). At 30 days of age, there were RPE abnormalities in *Tmem135* TG mice, such as vacuoliza-

Investigative Ophthalmology & Visual Science

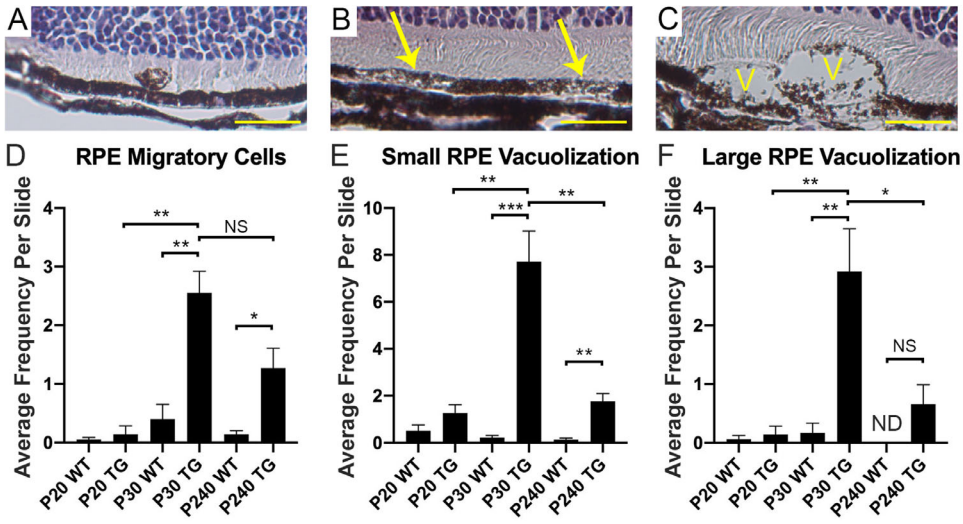

Figure 3. RPE pathologies in *Tmem135* TG mice. Representative images of P30 *Tmem135* TG RPE (**A–C**). RPE pathologies in *Tmem135* TG mice include migratory RPE cells (**A**) and vacuoles in RPE that were small (**B**, *yellow arrows*) and large (**C**). Magnification = 40X. *Scale bar* = 100 µm. (**D–F**) Quantification of migratory RPE cells, small and large RPE vacuolization in WT and *Tmem135* TG mice. There were significant increases in these RPE pathologies in P30 and P240 *Tmem135* TG mice although large RPE vacuolization in P240 *Tmem135* TG mice did not reach statistical significance. There were significant increases in these RPE pathologies between P20 and P30 *Tmem135* TG mice. Small and large RPE vacuolization significantly decreased between P30 and P240 *Tmem135* TG mice. Data from $n = 8$ WT (P20), $n = 7$ *Tmem135* TG (P20), $n = 5$ WT (P30), $n = 6$ *Tmem135* TG (P30), $n = 4$ WT (P240), and $n = 6$ *Tmem135* TG (P240). $^{*}P < 0.05$, $^{**}P < 0.01$, and $^{***}P < 0.001$, ANOVA. All data are mean ± SEM. ND, not detected; NS, not significant; V, vacuole.

tion, that were absent in WT mice (Fig. 2A, arrow). These pathologies along with RPE degeneration were noted in 240-day-old *Tmem135* TG mice (Fig. 2A). We measured the thickness of the RPE to quantify RPE degeneration. No differences were found in the RPE thickness between WT and *Tmem135* TG mice at 20 and 30 days of age (Figs. 2B, 2C). At 240 days of age, there were significant decreases in the RPE height in *Tmem135* TG mice compared with WT mice (Fig. 2D). We normalized the ONL thickness (ONLT) to the INL thickness to generate the ONLT ratio to investigate if there is photoreceptor degeneration in the *Tmem135* TG mice. We detected no differences in the ONLT ratios between *Tmem135* TG and WT mice at 20, 30, and 240 days of age (Figs. 2E–G). Our survey of *Tmem135* TG eyes revealed signs of RPE degeneration but no signs of photoreceptor degeneration.

We further investigated the type and extent of RPE pathologies in 30-day-old *Tmem135* TG mice. At this age, several changes were noted in the RPE of *Tmem135* TG mice including migratory cells (Fig. 3A), and small (Fig. 3B) and large vacuolization (Fig. 3C). We examined whether the migratory cells were subretinal immune cells engulfing sick RPE cells by labeling 30-day-old WT and *Tmem135* TG retinal cryosections with anti-IBA-1 (Supplementary Fig. S1). We did not see any IBA-1 positive immune cells in the subretinal space of 30-day-old *Tmem135* TG eyes (Supplementary Fig. S1), suggesting that these migratory cells are RPE cells. The frequency of the RPE pathologies were quantified for each 20-, 30- and 240-day-old WT and *Tmem135* TG mouse eye. Our analysis revealed that the frequency of RPE migratory cells were not different between 20-day-old WT and *Tmem135* TG mice but significantly increased in 30- and 240-day-old *Tmem135* TG mice compared with WT mice (Fig. 3D). We observed a similar trend in the frequency of small and large RPE vacuolization in 240-day-old *Tmem135* TG mice (Figs. 3E, 3F), although the increase in extensive RPE vacuolization does not reach statistical significance ($P = 0.15$) (Fig. 3F). Interestingly, there were significant decreases in the frequency of small and large RPE vacuolization in 240-day-old *Tmem135* TG mice compared with 30-day-old *Tmem135* TG mice (Figs. 3E, 3F), which may be due to RPE degeneration that occurs between these time points. In summary, overexpression of *Tmem135* leads to a variety of RPE pathologies.

Size and Density of RPE Cells in *Tmem135* TG Mice

RPE degeneration and abnormalities correlate with RPE dysmorphogenesis, including disorganization and enlargement of RPE cells in mice.[21,22] To determine if there is RPE dysmorphogenesis in the *Tmem135* TG eyes, we prepared and labeled RPE flat mounts from 20-, 30- and 240-day-old mice with an antibody against the tight junction-associated protein ZO-1 to delineate RPE cells and DAPI to stain nuclei. The RPE of 20-day-old *Tmem135* TG and WT mice were indistinguishable in their morphology and size (Fig. 4A). Conversely, there was disorganization of the RPE in 30- and 240-day-old *Tmem135* TG mice with loss of their classic hexagonal patterning (Fig. 4A). Analysis of RPE cell size revealed similar averages between 20-day-old *Tmem135* TG and WT mice (Fig. 4B). At 30 and 240 days of age, there was a significant increase in RPE cell size in *Tmem135* TG mice relative to WT mice (Fig. 4B). We observed significant increases in *Tmem135* TG RPE cell size across the ages used in this study (Fig. 4B). Evaluation of RPE cell density uncovered similar densities between *Tmem135* TG and WT mice at 20 days of age (Fig. 4C). It significantly decreased in *Tmem135* TG mice compared with age-matched WT mice at

Investigative Ophthalmology & Visual Science

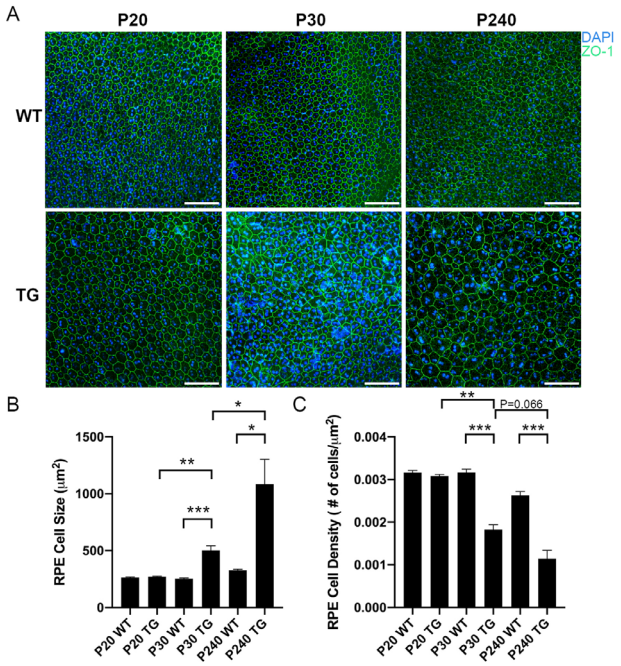

Figure 4. RPE dysmorphogenesis and cell enlargement in WT and *Tmem135* TG mice. (**A**) Representative images of WT and *Tmem135* TG RPE flat mounts at P20, P30, and P240 with ZO-1 in *green* and DAPI in *blue*. Magnification = 20X. *Scale bar* = 100 μm. (**B**) RPE cell size and (**C**) RPE cell density in WT and *Tmem135* TG mice. The RPE cell size in P30 and P240 *Tmem135* TG mice were greater than WT mice. The RPE cell density in P30 and P240 *Tmem135* TG mice were smaller than WT mice. There were age-dependent increases in RPE cell size and decreases in RPE cell density in *Tmem135* TG mice. Data from $n = 6$ WT (P20), $n = 4$ *Tmem135* TG (P20), $n = 4$ WT (P30), $n = 4$ *Tmem135* TG (P30), $n = 4$ WT (P240), and $n = 6$ *Tmem135* TG (P240). $^{*}P < 0.05$, $^{**}P < 0.01$, and $^{***}P < 0.001$, ANOVA. All data are mean ± SEM.

30 and 240 days of age (Fig. 4C). We found RPE cell density decreased in *Tmem135* TG mice between the ages examined in this experiment (Fig. 4C, a statistically significant change between P20 and P30 TG, and a decreasing trend between P30 and P240 TG [$P = 0.066$]). Together, these analyses showed that *Tmem135* TG mice have progressive RPE dysmorphogenesis and cell enlargement.

Ultrastructure of the RPE in *Tmem135* TG mice

EM was undertaken to visualize if there were ultrastructural abnormalities in *Tmem135* TG RPE (Fig. 5A). This analysis showed the presence of migratory RPE cells (Supplementary Fig. S2A); hyperpigmented RPE cells (Supplementary Fig. S2B); and small (Supplementary Fig. S2C), medium (Supplementary Fig. S2D), and large vacuolization (Supplementary Fig. S2E) within RPE cells of 60-day-old *Tmem135* TG mice. These pathologies were not observed in WT RPE at 60 days of age. We delved deeper into the *Tmem135* TG RPE phenotype by assessing mitochondria, pigment granules, and BrM thickness using a previously described systematic method to quantitate ocular pathologies in mice using EM.[23] In brief, retinal sections were mounted on 400-nm mesh thin bar grids, and images were taken at every place where a grid line intersected the RPE. We counted the number of mitochondria per image and found significantly reduced mitochondria in *Tmem135* TG RPE (Fig. 5B). Measurement of the mitochondrial surface area revealed significantly smaller mitochondria in *Tmem135* TG RPE compared with WT controls (Fig. 5C). Because there were hyperpigmented RPE in *Tmem135* TG eyes, we counted the number of pigment granules per image and saw a trend of increased pigment granules that did not reach statistical significance ($P = 0.07$) (Fig. 5D). The thickness of BrM was measured on each EM image, which was similar between WT and *Tmem135* TG (Fig. 5E). Through our ultrastructural examination of *Tmem135* TG RPE, we found the presence of basal laminar deposits, a pathological hallmark often seen in aged WT[24] and AMD mouse models,[25] in 10% of the *Tmem135* TG RPE images (Fig. 5F). These data show overexpression of *Tmem135* affects RPE ultrastructure in mice.

Visual Function Analysis of *Tmem135* TG Mice

Although we did not observe photoreceptor degeneration, we sought to investigate whether photoreceptor activity was affected by the RPE pathologies in the *Tmem135* TG mice. To examine photoreceptor activity, we measured the ERG responses of dark-adapted 60-, 180- and 365-day-old *Tmem135* TG and WT mice. There were no changes in the scotopic a- or b-wave in *Tmem135* TG and WT mice at 60 days (Figs. 6A, 6B) and 180 days (Figs. 6D, 6E) of age. We also detected no differences in the photopic a- and b-wave responses at 60 days of age in these genotypes (Supplementary Figs. S3A, S3B). At 180 days of age, although the photopic a-wave was not different (Supplementary Fig. S3C), there was a significant decrease in the photopic b-wave of *Tmem135* TG mice relative to WT mice at the 10 cd.s/m^2 flash intensity (Supplementary Fig. S3D). In 365-day-old *Tmem135* TG mice, the scotopic a-wave responses were significantly decreased at the 0.30, 1.00, and 30.00 cd.s/m^2 intensities (Fig. 6G), and the scotopic b-wave responses were significantly lowered at the 0.3 cd.s/m^2 through 3.0 cd.s/m^2 intensities (Fig. 6H). The photopic a-wave (Supplementary Fig. S3E) and b-wave (Supplementary Fig. S3F) did not differ between *Tmem135* TG and WT mice at 365 days of age. The c-wave of *Tmem135* TG mice were only significantly decreased at 365 days of age compared with age-matched control, but not earlier (Figs. 6C, 6F, 6I). We conclude that the visual function of *Tmem135* TG mice remains generally intact past 180 days of age, and show decreased scotopic a-, b-, and c-wave responses by 365 days of age.

RPE and Photoreceptor Markers in Aged *Tmem135* TG mice

To test whether there was photoreceptor degeneration along with RPE degeneration in *Tmem135* TG mice at 365 days of age in which there are differences in ERG responses, we isolated RNA from separated eyecups and neural retinas from 365-day-old *Tmem135* TG and WT mice for quantitative PCR (qPCR) measuring RPE markers (retinaldehyde binding protein 1 [*Rblp1*], bestrophin 1 [*Best1*], and potassium inwardly rectifying channel subfamily J member 13 [*Kcnj13*]) and photoreceptor markers (rhodopsin [*Rho*], opsin 1 short wave sensitive [*Opn1 sw*], opsin 1 medium wave sensitive [*Opn1 mw*], arrestin 3 [*Arr3*], G protein subunit alpha transducin 2 [*Gnat2*], elongation of very long-chain fatty acids-like 4 [*Elovl4*], adenosine triphosphatase [ATP] binding cassette subfamily A member 4 [*Abca4*], retinal degeneration slow [*Rds*], surface antigen protein 1 [*Sag1*], G

Investigative Ophthalmology & Visual Science

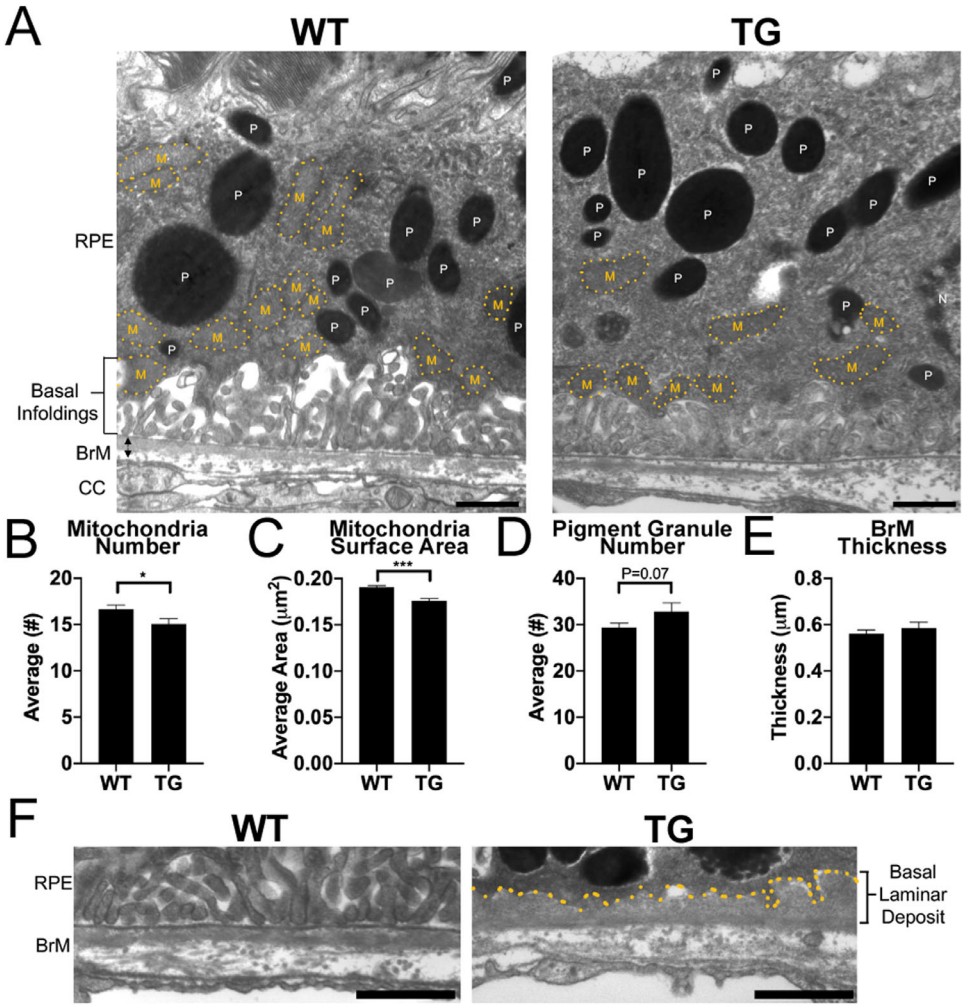

Figure 5. Ultrastructure of WT and *Tmem135* TG RPE. (**A**) Representative EM images of 60-day-old WT and *Tmem135* TG RPE. Mitochondria (M), pigment granules (P), and nucleus (N) are labeled. Mitochondrial surface area is outlined in *yellow*. BrM thickness is delineated by *black arrows*. Magnification = 15,000X. *Scale bar* = 800 nm. CC, choriocapillaris. Quantification of mitochondria number (**B**), mitochondrial surface area (**C**), pigment granule number (**D**), and BrM thickness (**E**) per EM image. We measured the surface area of 3057 mitochondria in WT RPE and 1730 mitochondria in *Tmem135* TG RPE. There were fewer and smaller mitochondria in *Tmem135* TG RPE at 60 days of age. All data are mean ± SEM. (**F**) Representative EM images of basal laminar deposits in *Tmem135* TG mice. Basal laminar deposit is outlined in *yellow*. Some 10% of *Tmem135* TG EM images had basal laminar deposits. Data from $n = 3$ WT (P60), $n = 3$ *Tmem135* TG (P60). $^{*}P < 0.05$ and $^{***}P < 0.001$, ANOVA. All data are mean ± SEM.

protein subunit alpha transducin 1 [*Gnat1*], and retinal outer segment membrane protein 1 [*Rom1*]). There were significant decreases in *Rblp1*, *Best1,* and *Kcnj13,* but no changes in any of the photoreceptor markers (Fig. 7A). We confirm our qPCR results through Western blot analysis in which there were significant decreases in CRALBP in the eyecups (Fig. 7B) and no changes in RHO in the neural retinas (Fig. 7C) of 365-day-old *Tmem135* TG mice. Our data suggest that there is no significant photoreceptor degeneration in TG mice at 365 days of age.

RPE in *Tmem135* Mutant Mice

Given that the RPE of *Tmem135* TG mice exhibited numerous abnormalities, we revisited RPE phenotypes in $Tmem135^{FUN025/FUN025}$ mutant mice. Our previous study found photoreceptor degeneration, infiltration of immune cells into the subretinal space, RPE hypertrophy, and visual loss in $Tmem135^{FUN025/FUN025}$ mice relative to WT mice.[8] Age-dependent photoreceptor degeneration, subretinal immune cells, and RPE hypertrophy were observed in $Tmem135^{FUN025/FUN025}$ mice compared with $Tmem135^{FUN025/+}$ littermate controls at 45 and 365 days of age (Supplementary Fig. S4) consistent with our previous report.[8] Photoreceptor degeneration in 365-day-old $Tmem135^{FUN025/FUN025}$ translated into lowered scotopic ERG a-wave (Supplementary Fig. S5A) and b-wave (Supplementary Fig. S5B) responses, although the changes in the scotopic b-wave did not reach significance. The c-wave (Supplementary Fig. S5C), photopic a-wave (Supplementary Fig. S5D), and b-wave (Supplementary Fig. S5E) were significantly attenuated in $Tmem135^{FUN025/FUN025}$ mice compared with $Tmem135^{FUN025/+}$ mice.

We evaluated RPE phenotypes of $Tmem135^{FUN025/+}$ and $Tmem135^{FUN025/FUN025}$ mice at 45 and 365 days of age. RPE flat-mount analysis showed no signs of RPE dysmorphogen-

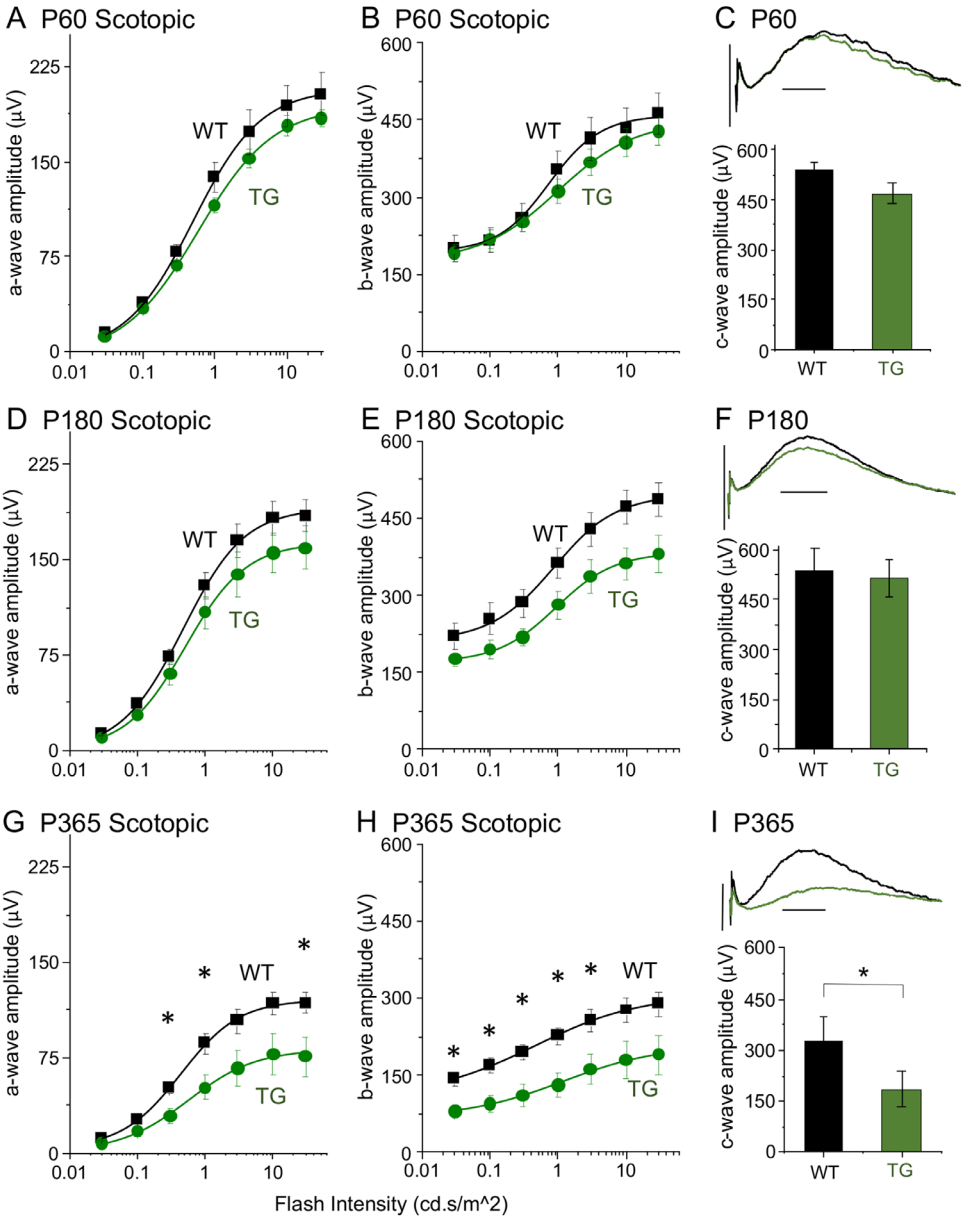

Figure 6. Visual function in WT and *Tmem135* TG mice. Transcorneal ERG recordings for P60 (**A–C**), P180 (**D–F**), and P365 (**G–I**) WT and *Tmem135* TG mice. No significant changes were noted in the scotopic a-, scotopic b-, and c-waves at P60 and P180 between these genotypes. There were significant decreases in the scotopic a- and b-wave at some light intensities, as well as the c-wave of P365 *Tmem135* TG mice compared with WT mice. Data from $n = 5$ WT (P60), $n = 10$ *Tmem135* TG (P60), $n = 5$ WT (P180), $n = 3$ *Tmem135* TG (P180), $n = 5$ WT (P365), and $n = 4$ *Tmem135* TG (P365). *$P < 0.05$, ANOVA. All data are mean ± SEM.

esis in *Tmem135*$^{FUN025/FUN025}$ mice (Fig. 8A). Quantification of the RPE flat mounts revealed decreased cell size (Fig. 8A) and increased cell density (Fig. 8B) in *Tmem135*$^{FUN025/FUN025}$ mice compared with *Tmem135*$^{FUN025/+}$ mice at 45 and 365 days of age. These findings show that the *Tmem135* mutation affects RPE cells differently than the overexpression of *Tmem135*.

Mitochondrial Morphology in RPE

The RPE phenotypes in *Tmem135* TG and *Tmem135*$^{FUN025/FUN025}$ mice mirror the overly fragmented and fused mitochondrial phenotypes in primary-cultured mouse fibroblasts from these mice, respectively.[8] To evaluate the mitochondrial morphologies in RPE cells, we isolated and cultured mouse RPE cells from 60-day-old WT, *Tmem135* TG, and *Tmem135*$^{FUN025/FUN025}$ mice. We verified our cell cultures for tight junctions and RPE protein expression (Supplementary Fig. S6). Using these cultures, we stained the RPE cells with Mitotracker (Thermo Fisher Scientific, Waltham, MA, USA) to visualize the mitochondria. We found normal mitochondria in WT RPE cells (Fig. 9A) but overly fragmented mitochondria in *Tmem135* TG RPE cells (Fig. 9B) and overly fused mitochondria in *Tmem135*$^{FUN025/FUN025}$ RPE cells (Fig. 9C). Therefore the RPE phenotypes in *Tmem135* TG and *Tmem135*$^{FUN025/FUN025}$ mice are associated with mitochondria morphological changes.

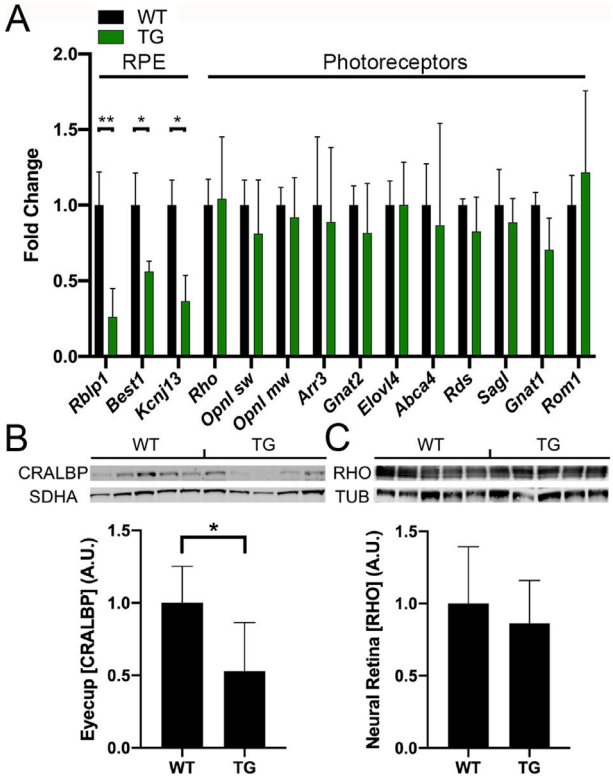

Figure 7. RPE and photoreceptor markers in 365-day-old WT and *Tmem135* TG mice. (**A**) Quantitative PCR analysis of RPE and photoreceptor markers revealed decreased RPE but not photoreceptor markers. Values in *Tmem135* TG mice are normalized against those of WT mice. $n = 3$ for each genotype. (**B**) Western blot analysis of eyecup lysates of 365-day-old WT and *Tmem135* TG mice for cellular retinaldehyde-binding protein (CRALBP). $N = 5$. (**C**) Western blot analysis of neural retinal lysates of 365-day-old WT and *Tmem135* TG mice for rhodopsin (RHO). $N = 5$. Succinate dehydrogenase A (SDHA) and tubulin (TUB) served as loading controls for eyecup and neural retina lysate blots, respectively. $^{*}P < 0.05$ and $^{**}P < 0.01$, ANOVA. All data are mean ± SD.

Oxidative Phosphorylation Proteins in *Tmem135* TG and *Tmem135*$^{FUN025/FUN025}$ Tissues

Mitochondria modify their morphology through mitochondrial dynamics to sustain energy homeostasis within cells.[26] To test whether there was altered mitochondrial energy production in *Tmem135* TG and *Tmem135*$^{FUN025/FUN025}$ mice, we evaluated the levels of proteins involved in mitochondrial oxidative phosphorylation (OXPHOS), the main source of cellular ATP.[27] Using a commercially available antibody cocktail, we examined the protein levels of ATP synthase subunit alpha (ATP5A), cytochrome b-c1 complex subunit 2 (UQCRC2), cytochrome c oxidase subunit 1 (MTCO1), succinate dehydrogenase subunit B (SDHB), and NADH dehydrogenase beta subcomplex subunit 8 (NDUFB8) in eyecup and neural retina lysates of 365-day-old WT, *Tmem135* TG, *Tmem135*$^{FUN025/+}$, and *Tmem135*$^{FUN025/FUN025}$ mice. We found no changes in OXPHOS proteins in *Tmem135* TG eyecups versus WT littermates (Fig. 10A) and *Tmem135*$^{FUN025/FUN025}$ eyecups relative to *Tmem135*$^{FUN025/+}$ (Fig. 10B). In the *Tmem135* TG neural retinas, we measured significant decreases in ATP5A, UQCRC2, MTCO1, SDHB, and NDUFB8 compared with WT (Fig. 10C). In contrast, there were significant increases in ATP5A and UQCRC2 in the *Tmem135*$^{FUN025/FUN025}$ neural retinas (Fig. 10D). As a positive control, we quantitated the level of these OXPHOS proteins in heart lysates because expression of OXPHOS genes is decreased in *Tmem135* TG hearts.[13] There were significant decreases in ATP5A, UQCRC2, MTCO1, and SDHB in *Tmem135* TG hearts (Fig. 10E) but significant increases in ATP5A, UQCRC2, and NDUFB8 in *Tmem135*$^{FUN025/FUN025}$ hearts (Fig. 10F). Our results indicate that *Tmem135* overexpression and mutation leads to changes in mitochondrial OXPHOS.

Discussion

Imbalanced mitochondrial dynamics are thought to accumulate dysfunctional mitochondria and contribute to aging and disease.[28] In support of this hypothesis, we identified *Tmem135* as a gene important in regulating mitochondrial dynamics, maintaining the mitochondrial function, and inhibiting the formation of age-dependent retinal pathologies in mice.[8,13] Our current study furthers our understanding of TMEM135 biology by phenotyping the eyes of *Tmem135* TG mice. In *Tmem135* TG mice, the full-length murine *Tmem135* cDNA is driven by a chicken beta-actin promoter, which results in overexpression of *Tmem135* in the eyecup and neural retina at equal levels. However, we detect pathologies only in the RPE, including degeneration, vacuolization, migration, dysmorphogenesis, and cell enlargement. In contrast, the neural retina does not appear to be sensitive to the upregulation of *Tmem135,* as we did not observe any pathologies in the retinas of *Tmem135* TG mice. The dampened scotopic ERG a- and b-waves in 365-day-old *Tmem135* TG mice is more likely due to functional RPE deficits, as shown by significant reduction of c-wave response. Our qPCR analysis uncovered a decrease of both *Kcnj13* and *Best1* expression in *Tmem135* TG eyecups but not in photoreceptor genes in *Tmem135* TG neural retinas relative to WT tissues. *Kcnj13* encodes Kir7.1 channel critical for the efflux of potassium ions and generation of the RPE-derived c-wave.[29] Hence a decrease in *Kcnj13* would explain the reduced c-wave and scotopic ERG responses in *Tmem135* TG mice because their RPE is unable to restore potassium ions in the subretinal space required for visual transduction.[30] However, the *Tmem135*^{FUN025} mutation leads to contrasting changes in the RPE. *Tmem135*^{FUN025} mutant mice have thicker, smaller, and denser RPE, whereas their photoreceptor cells progressively degenerate.[8] Thus we conclude that the balance of functional TMEM135 is essential for RPE health.

The RPE phenotypes of *Tmem135* TG and *Tmem135*^{FUN025} mutant mice correlate with disruptions in mitochondrial dynamics. We confirm smaller mitochondria in EM images of 60-day-old *Tmem135* TG RPE that is in contrast with our previous study finding larger mitochondria in EM images of *Tmem135*^{FUN025} mutant RPE.[8] These results are consistent with the mitochondrial staining of primary-cultured RPE indicating overly fragmented mitochondria in *Tmem135* TG RPE and overly fused mitochondria in *Tmem135*^{FUN025} mutant RPE. Mitochondrial dynamics is essential for mitochondrial homeostasis and thought to contribute to tissue aging,[31] although it is unknown whether mitochondrial dynamics affects RPE aging. It has been postulated that mitochondrial fission facilitates the removal of damaged mitochondrial membranes to preserve mitochondrial function.[32,33] Overfragmentation of mitochondria due to *Tmem135* overexpression may

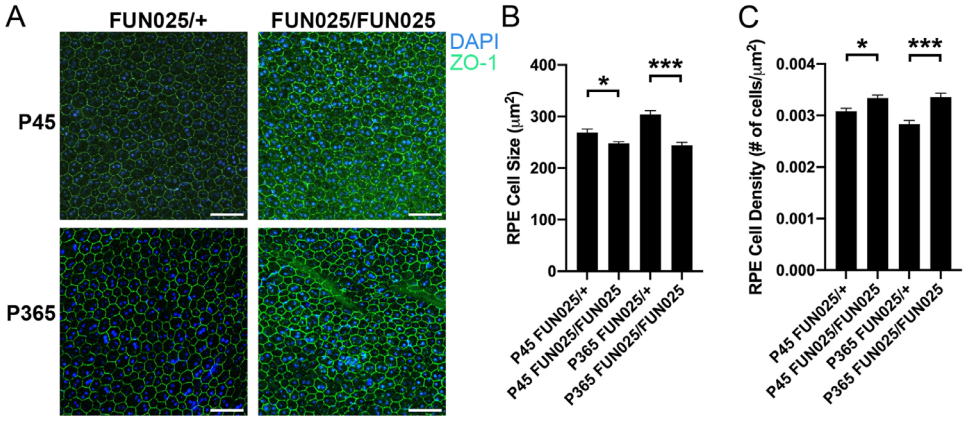

Figure 8. RPE size and density in *Tmem135*$^{FUN025/+}$and *Tmem135*$^{FUN025/FUN025}$ mice. (**A**) Representative images of P45 and P365 *Tmem135*$^{FUN025/+}$ and *Tmem135*$^{FUN025/FUN025}$ RPE flat mounts with ZO-1 in *green* and DAPI in *blue*. Magnification = 20X. *Scale bar* = 100 μm. (**B**) RPE cell size and (**C**) RPE cell density in *Tmem135*$^{FUN025/+}$ and *Tmem135*$^{FUN025/FUN025}$ mice. The RPE cell size in P45 and P240 *Tmem135*$^{FUN025/FUN025}$ mice were greater than *Tmem135*$^{FUN025/+}$control mice. The RPE cell density in P45 and P240 *Tmem135*$^{FUN025/FUN025}$ mice were smaller than *Tmem135*$^{FUN025/+}$control mice. Data from $n = 4$ *Tmem135*$^{FUN025/+}$ (P45), $n = 4$ *Tmem135*$^{FUN025/FUN025}$ (P45), $n = 9$ *Tmem135*$^{FUN025/+}$ (P365), and $n = 10$ *Tmem135*$^{FUN025/FUN025}$ (P365). *$P < 0.05$ and ***$P < 0.001$, ANOVA. All data are mean ± SEM.

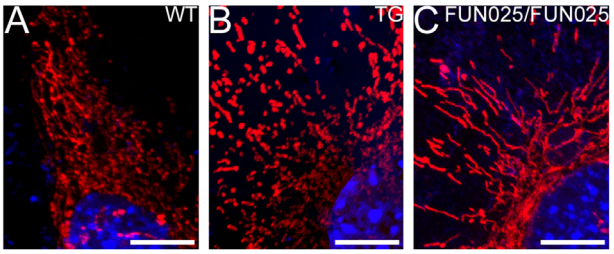

Figure 9. Mitochondrial morphology in primary RPE cultures. Representative images of mitochondria (*red*) and nucleus (*blue*) in RPE cells obtained from 60-day-old (**A**) WT, (**B**) *Tmem135* TG, and (**C**) *Tmem135*$^{FUN025/FUN025}$ mice. Note the fragmented mitochondria in the *Tmem135* TG RPE cell, and elongated mitochondria in the *Tmem135*$^{FUN025/FUN025}$ RPE cell. Magnification = 60X. *Scale bar* = 10 μm.

result in mitochondrial dysfunction in the RPE, which in turn could lead to RPE degeneration. Consistent with this hypothesis, loss of mitochondrial function in the RPE either by ablating the mitochondrial transcription factor *Tfam* or mitochondrial biogenesis gene *Pgc-1α* leads to RPE degeneration.[21,34] On the contrary, mitochondrial fusion is thought to intermix proteins and DNA between mitochondria under conditions of nutrient deprivation.[35] Enhancing mitochondrial fusion in *Tmem135*^{FUN025} mutant mice may trigger increased nutrient intake and metabolic stress in the RPE that causes RPE thickening. In support of this idea, a nuclear magnetic resonance–based metabolomics study revealed an accumulation of metabolites linked to glucose, amino acid, and fat metabolic pathways in primary-cultured *Tmem135*^{FUN025} mutant RPE cells compared with WT and *Tmem135* TG RPE cells.[20] Furthermore, inducing metabolic stress through hypoxia[36] or oxidative stress[37] can cause thickening of the RPE in mice, similarly to what we observe in *Tmem135*^{FUN025} mutant mice. RPE phenotypes of *Tmem135* TG and *Tmem135*^{FUN025} mutant mice align with other published reports of RPE phenotypes in mice with known mitochondrial dysfunction, a cellular consequence of aging.[4]

Although it is clear that TMEM135 is important in mitochondrial dynamics, how mitochondrial dynamics is regulated by TMEM135 at the molecular level is unknown. Although TMEM135 may function at mitochondria to regulate their dynamics by associating with fission/fusion machineries, it is also possible that TMEM135 is involved in a different mechanism at mitochondria, which influences mitochondrial dynamics. In this study, we found that *Tmem135* overexpression and mutation lead to changes in the level of mitochondrial OXPHOS proteins, which could be related to TMEM135 function at mitochondria. It has been shown that increased OXPHOS stimulates mitochondrial fusion,[38] whereas inhibition of OXPHOS by drug treatments are associated with enhanced mitochondrial fission.[39] However, dysregulated mitochondrial dynamics can also lead to changes in OXPHOS,[39] which may be more likely in this case considering the following findings. We observed decreased OXPHOS proteins in *Tmem135* TG neural retina and heart lysates, as well as increased OXPHOS proteins in *Tmem135*^{FUN025} mutant neural retina and heart lysates, whereas we did not detect changes in OXPHOS proteins in the *Tmem135* TG and *Tmem135*^{FUN025} mutant eyecup (RPE/choroid/sclera). The fact that we observed mitochondrial shape/size changes in *Tmem135* TG and mutant RPE, but not OXPHOS changes, points to the scenario that TMEM135 function is more closely related to mitochondrial dynamics, which in turn influences OXPHOS in some tissues but not in the RPE. However, it is also possible that the heterogeneity of the eyecup tissue that includes the RPE, choroid, sclera, and choroidal immune cells, masked OXPHOS changes in the RPE alone. It is interesting to note that no pathologies were observed in the neural retina of *Tmem135* TG mice in which OXPHOS proteins were significantly decreased. This may be explained by the metabolic pathway photoreceptor cells use to meet their energy demands. Photoreceptor cells are known to largely depend on aerobic glycolysis as the source of ATP,[40] and therefore the decrease in OXPHOS proteins may have less effect on the energy demand of these cells. In contrast, it is well established that the RPE relies on OXPHOS to utilize lactate produced by the photoreceptors[41] and fatty acids derived from photoreceptor outer segments.[42] Thus if there

Investigative Ophthalmology & Visual Science

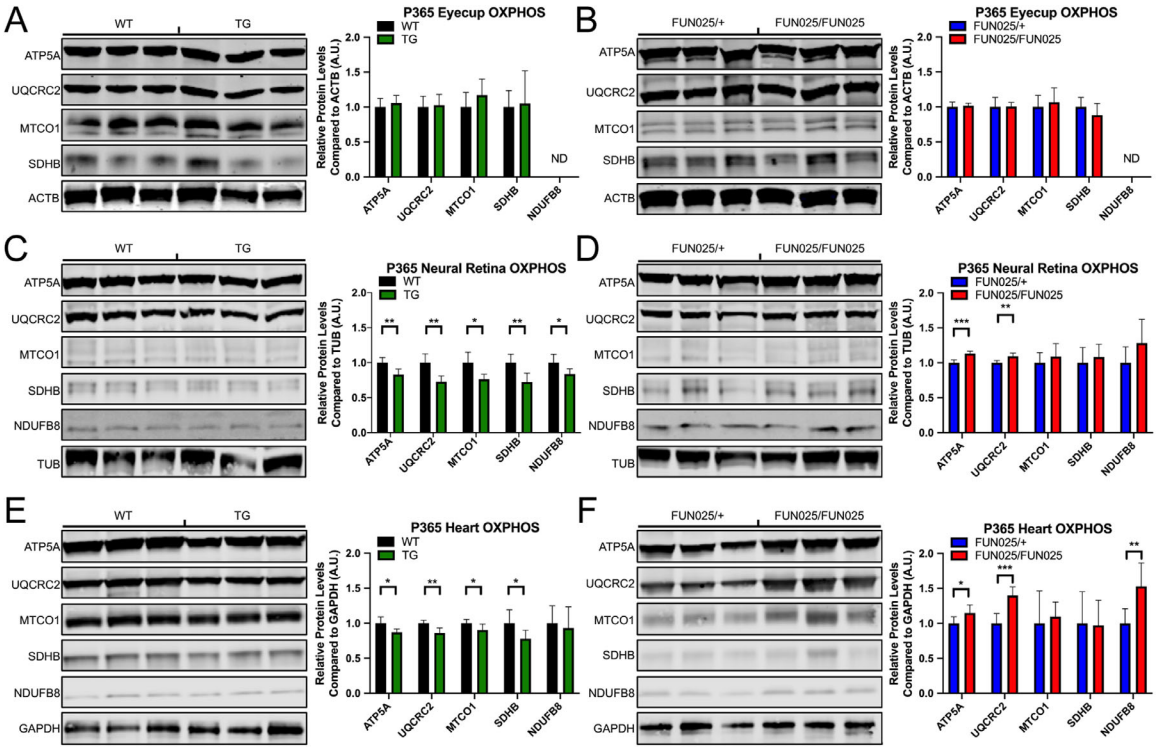

Figure 10. Relative levels of OXPHOS proteins in 365-day-old *Tmem135* TG and *Tmem135*$^{FUN025/FUN025}$ tissues. Representative Western blots for ATP synthase subunit alpha (ATP5A), cytochrome b-c1 complex subunit 2 (UQCRC2), cytochrome c oxidase subunit 1 (MTCO1), succinate dehydrogenase subunit B (SDHB), and NADH dehydrogenase beta subcomplex subunit 8 (NDUFB8) using eyecup lysates (**A,B**), neural retina lysates (**C,D**) and heart lysates (**E,F**) for WT and *Tmem135* TG (**A,C,E**) as well as *Tmem135*$^{FUN025/+}$ and *Tmem135*$^{FUN025/FUN025}$ mice (**B,D,F**). We did not detect NDUFB8 on our Western blots containing eyecup lysates, which may be owing to the lower protein concentrations used for these blots. Immunobands were normalized to loading control. Beta-actin (ACTB), tubulin (TUB), and glyceraldehyde 3-phosphate dehydrogenase (GAPDH) served as loading controls for eyecup, neural retina, and heart blots, respectively. Data from *Tmem135* TG were normalized to WT and *Tmem135*$^{FUN025/FUN025}$ were normalized to *Tmem135*$^{FUN025/+}$. $N = 5–7$. All information on the samples used for these Western blots are included in Supplementary Tables S1 and S2. ND, not detected. $^{*}P < 0.05$, $^{**}P < 0.01$, and $^{***}P < 0.001$, ANOVA. All data are mean ± SD.

is indeed a decrease in OXPHOS in the RPE of *Tmem135* TG mice concealed by the tissue heterogenuity of the eyecup as discussed earlier, then such a change in OXPHOS may have detrimental effects on RPE cells.

It is also important to note that the TMEM135 protein was not always localized on mitochondria in our previous report.[8] TMEM135 was also observed as punctate signals in the cytosol, which may represent vesicle-like structures.[8] This observation led us to hypothesize that TMEM135 may be trafficked between mitochondria and cytosolic vesicles. Peroxisomes are one of such cytosolic vesicles in which TMEM135 was previously localized[10,11] and may be involved in the potential mechanism through which TMEM135 regulates mitochondrial dynamics. Physical contacts between peroxisomes and mitochondria have been well studied,[43,44] and more importantly, a recent study indicated that mitochondrial fission could be regulated by peroxisomes.[45] Based on these notions, it is possible that TMEM135 functions in peroxisomes and its perturbation may, in turn, affect mitochondrial dynamics. Alternatively, TMEM135 may have multiple molecular functions, and RPE phenotypes we have observed may be in part caused by a defect in a different function/pathway. Maharjan et al.[11] reported that TMEM135 might be a regulator of Rab8-mediated primary ciliogenesis in cultured RPE1 cells. However, this function could also be connected with mitochondrial function, which has been shown to dictate the length of cilia.[46] TMEM135 could also play a role in lipid metabolism. TMEM135 increases in the hearts of mitochondrial very-long-chain acyl-CoA dehydrogenase (*Vlcad*) deficient mice that lack the ability to break down very-long-chain fatty acids through mitochondrial ß-oxidation.[10] These mice show lipid accumulation in the heart, as well as cardiac pathologies, including collagen deposition, vacuolated myocytes, and abnormal mitochondrial morphology,[47] which are similar to heart pathologies in *Tmem135* TG mice. Further molecular analysis may help us to understand the molecular function of TMEM135 in RPE cells.

Structural changes in the RPE of *Tmem135* TG mice, including pigmentary changes, migratory cells, dysmorphogenesis, degeneration, are often observed in patients with AMD,[48–50] which is a common and complex photoreceptor degenerative disease strongly conferred by advanced aging but influenced by genetics and environmental stressors.[51] These RPE changes in the *Tmem135* TG mice are also similar to those observed in previous AMD mouse models, including sodium iodate–injected C57BL/6J,[52,53] *Dicer1* knockout,[22,54] *RPE*^{CreER}*/DTA*,[55] and *Sod2* knockout mice.[56–58] Interestingly, mitochondrial fragmentation has been documented to occur in human AMD donor eyes.[59] It is possible that upregulated TMEM135 activity may be involved in this mitochondrial fragmentation. Thus it will be valuable to evaluate TMEM135

expression and localization in AMD donor eyes to investigate whether there is a link between TMEM135 and AMD in a future study.

Conclusions

We have identified the pathogenic effects of *Tmem135* overexpression on mouse RPE cells. These RPE pathologies contrast those in *Tmem135*^{FUN025} mutant mice consisting of thicker, smaller, and denser RPE. These divergent RPE phenotypes correlate with contrasting mitochondrial sizes and morphologies (overfragmented vs. overfused) in RPE cells due to *Tmem135* overexpression and mutation. This study demonstrated that TMEM135-regulated mitochondrial dynamics are critical for the health of RPE in mice.

Acknowledgments

The authors thank Satoshi Kinoshita and the University of Wisconsin Translational Research Initiatives in Pathology laboratory (TRIP), supported by the University of Wisconsin Department of Pathology and Laboratory Medicine, UWCCC (P30 CA014520) and the Office of the Director, National Institutes of Health (S10OD023526) for the use of facilities and services, as well as Randall Massey and the University of Wisconsin Electron Microscope Core for tissue processing, sectioning, and assistance for this study. The authors also want to recognize Freya Mowat and Janis Eells for their advice and feedback on this work.

Supported by grants NIH R01 EY022086, R01EY024995, Timothy William Trout Chairmanship, NIH T32EY027721, NIH P30 EY016665, M.D. Matthews Research Professorship, and an Unrestricted Grant from Research to Prevent Blindness, Inc.

Disclosure: **M. Landowski,** None; **S. Grindel,** None; **P.K. Shahi,** None; **A. Johnson,** None; **D. Western,** None; **A. Race,** None; **F. Shi,** None; **J. Benson,** None; **M. Gao,** None; **E. Santoirre,** None; **W.-H. Lee,** None; **S. Ikeda,** None; **B.R. Pattnaik,** None; **A. Ikeda,** None

References

1. Lambert NG, ElShelmani H, Singh MK, et al. Risk factors and biomarkers of age-related macular degeneration. *Prog Retin Eye Res*. 2016;54:64–102.
2. Yau JW, Rogers SL, Kawasaki R, et al. Global prevalence and major risk factors of diabetic retinopathy. *Diabetes Care*. 2012;35:556–564.
3. McMonnies CW. Glaucoma history and risk factors. *J Optom*. 2017;10:71–78.
4. López-Otín C, Blasco MA, Partridge L, Serrano M, Kroemer G. The hallmarks of aging. *Cell*. 2013;153:1194–1217.
5. Wong WL, Su X, Li X, et al. Global prevalence of age-related macular degeneration and disease burden projection for 2020 and 2040: a systematic review and meta-analysis. *Lancet Glob Health*. 2014;2:e106–e116.
6. Tham YC, Li X, Wong TY, Quigley HA, Aung T, Cheng CY. Global prevalence of glaucoma and projections of glaucoma burden through 2040: a systematic review and meta-analysis. *Ophthalmology*. 2014;121:2081–2090.
7. Wong TY, Sabanayagam C. Strategies to tackle the global burden of diabetic retinopathy: from epidemiology to artificial intelligence. *Ophthalmologica*. 2020;243:9–20.
8. Lee WH, Higuchi H, Ikeda S, et al. Mouse Tmem135 mutation reveals a mechanism involving mitochondrial dynamics that leads to age-dependent retinal pathologies. *Elife*. 2016;5:1–29.
9. Žárský V, Doležal P. Evolution of the Tim17 protein family. *Biol Direct*. 2016;11:1–13.
10. Exil VJ, Silva Avila D, Benedetto A, et al. Stressed-induced TMEM135 protein is part of a conserved genetic network involved in fat storage and longevity regulation in *Caenorhabditis elegans*. *PLoS One*. 2010;5:e14228.
11. Maharjan Y, Lee JN, Kwak SA, et al. TMEM135 regulates primary ciliogenesis through modulation of intracellular cholesterol distribution. *EMBO Rep*. 2020;21:1–16.
12. Tilokani L, Nagashima S, Paupe V, Prudent J. Mitochondrial dynamics: overview of molecular mechanisms. *Essays Biochem*. 2018;62:341–360.
13. Lewis SA, Takimoto T, Mehrvar S, et al. The effect of Tmem135 overexpression on the mouse heart. *PLoS One*. 2018;13:e0201986.
14. Pittler SJ, Baehr W. Identification of a nonsense mutation in the rod photoreceptor cGMP phosphodiesterase beta-subunit gene of the RD mouse. *Proc Natl Acad Sci U S A*. 1991;88:8322–8326.
15. Mattapallil MJ, Wawrousek EF, Chan CC, et al. The Rd8 mutation of the Crb1 gene is present in vendor lines of C57BL/6N mice and embryonic stem cells, and confounds ocular induced mutant phenotypes. *Invest Ophthalmol Vis Sci*. 2012;53:2921–2927.
16. Livak KJ, Schmittgen TD. Analysis of relative gene expression data using real-time quantitative PCR and the 2(-Delta C(T)) Method. *Methods*. 2001;25:402–408.
17. Higuchi H, Macke EL, Lee WH, et al. Genetic basis of age-dependent synaptic abnormalities in the retina. *Mamm Genome*. 2015;26:21–32.
18. Bhatia SK, Rashid A, Chrenek MA, et al. Analysis of RPE morphometry in human eyes. *Mol Vis*. 2016;22:898–916.
19. Chen M, Muckersie E, Robertson M, Fraczek M, Forrester JV, Xu H. Characterization of a spontaneous mouse retinal pigment epithelial cell line B6-RPE07. *Invest Ophthalmol Vis Sci*. 2008;49:3699–3706.
20. Lee WH, Bhute VJ, Higuchi H, IkedaS, Palecek SP, Ikeda A. Metabolic alterations caused by the mutation and overexpression of the *Tmem135* gene [e-pub ahead of print]. *Exp Biol Med*, https://doi.org/10.1177/1535370220932856.
21. Zhao C, Yasumura D, Li X, et al. mTOR-mediated dedifferentiation of the retinal pigment epithelium initiates photoreceptor degeneration in mice. *J Clin Invest*. 2011;121:369–383.
22. Wright CB, Uehara H, Kim Y, et al. Chronic Dicer1 deficiency promotes atrophic and neovascular outer retinal pathologies in mice. *Proc Natl Acad Sci U S A*. 2020;117:2579–2587.
23. Ding JD, Kelly U, Landowski M, et al. Expression of human complement factor H prevents age-related macular degeneration-like retina damage and kidney abnormalities in aged CFH knockout mice. *Am J Pathol*. 2015;185:29–42.
24. Mori H, Yamada H, Toyama K, et al. Developmental and age-related changes to the elastic lamina of Bruch's membrane in mice. 2019;257:289–301.
25. Pennesi ME, Neuringer M, Courtney RJ. Animal models of age related macular degeneration. *Mol Aspects Med*. 2012;33:487–509.
26. Liesa M, Shirihai OS. Mitochondrial dynamics in the regulation of nutrient utilization and energy expenditure. *Cell Metab*. 2013;17:491–506.
27. Bonora M, Patergnani S, Rimessi A, et al. ATP synthesis and storage. *Purinergic Signal*. 2012;8:343–357.
28. Sebastián D, Palacín M, Zorzano A. Mitochondrial dynamics: coupling mitochondrial fitness with healthy aging. *Trends Mol Med*. 2017;23:201–215.
29. Shahi PK, Liu X, Aul B, et al. Abnormal electroretinogram after Kir7.1 channel suppression suggests role in retinal electrophysiology. *Sci Rep*. 2017;7:1–13.

30. Wu J, Peachey NS, Marmorstein AD. Light-evoked responses of the mouse retinal pigment epithelium. *J Neurophysiol*. 2004;91:1134–1142.
31. Liu YJ, McIntyre RL, Janssens GE, Houtkooper RH. Mitochondrial fission and fusion: a dynamic role in aging and potential target for age-related disease. *Mech Ageing Dev*. 2020;186:111212.
32. Wai T, Langer T. Mitochondrial dynamics and metabolic regulation. *Trends Endocrinol Metab*. 2016;27:105–117.
33. Zorov DB, Vorobjev IA, Popkov VA, et al. Lessons from the discovery of mitochondrial fragmentation (Fission): a review and update. *Cells*. 2019;8:1–17.
34. Rosales MAB, Shu DY, Iacovelli J, Saint-Geniez M. Loss of PGC-1α in RPE induces mesenchymal transition and promotes retinal degeneration. *Life Sci Alliance*. 2019;2:1–17.
35. Westermann B. Mitochondrial fusion and fission in cell life and death. *Nat Rev Mol Cell Biol*. 2010;11:872–884.
36. Kurihara T, Westenskow PD, Gantner ML, et al. Hypoxia-induced metabolic stress in retinal pigment epithelial cells is sufficient to induce photoreceptor degeneration. *Elife*. 2016;5:e14319.
37. Brown EE, DeWeerd AJ, Ildefonso CJ, Lewin AS, Ash JD. Mitochondrial oxidative stress in the retinal pigment epithelium (RPE) led to metabolic dysfunction in both the RPE and retinal photoreceptors. *Redox Biol*. 2019;24:101201.
38. Mishra P, Chan DC. Mitochondrial dynamics and inheritance during cell division, development and disease. *Nat Rev Mol Cell Biol*. 2014;15:634–646.
39. Mishra P, Chan DC. Metabolic regulation of mitochondrial dynamics. *J Cell Biol*. 2016;212:379–387.
40. Petit L, Ma S, Cipi J, et al. Aerobic glycolysis is essential for normal rod function and controls secondary cone death in retinitis pigmentosa. *Cell Rep*. 2018;23:2629–2642.
41. Kanow MA, Giarmarco MM, Jankowski CS, et al. Biochemical adaptations of the retina and retinal pigment epithelium support a metabolic ecosystem in the vertebrate eye. *Elife*. 2017;6:e28899.
42. Adijanto J, Du J, Moffat C, Seifert EL, Hurle JB, Philp NJ. The retinal pigment epithelium utilizes fatty acids for ketogenesis. *J Biol Chem*. 2014;289:20570–20582.
43. Valm AM, Cohen S, Legant WR, et al. Applying systems-level spectral imaging and analysis to reveal the organelle interactome. *Nature*. 2017;546:162–167.
44. Shai N, Yifrach E, van Roermund CWT, et al. Systematic mapping of contact sites reveals tethers and a function for the peroxisome-mitochondria contact. *Nat Commun*. 2018;9:1–13.
45. Tanaka H, Okazaki T, Aoyama S, et al. Peroxisomes control mitochondrial dynamics and the mitochondrion-dependent apoptosis pathway. *J Cell Sci*. 2019;132:1–15.
46. Burkhalter MD, Sridhar A, Sampaio P, et al. Imbalanced mitochondrial function provokes heterotaxy via aberrant ciliogenesis. *J Clin Invest*. 2019;129:2841–2855.
47. Exil VJ, Roberts RL, Sims H, et al. Very-long-chain acyl-coenzyme a dehydrogenase deficiency in mice. *Circ Res*. 2003;93:448–455.
48. Gambril JA, Sloan KR, Swain TA, et al. Quantifying retinal pigment epithelium dysmorphia and loss of histologic autofluorescence in age-related macular degeneration. *Invest Ophthalmol Vis Sci*. 2019;60:2481–2493.
49. Bird AC, Phillips RL, Hageman GS. Geographic atrophy: a histopathological assessment. *JAMA Ophthalmol*. 2014;132:338–345.
50. Zanzottera EC, Ach T, Huisingh C, Messinger JD, Spaide RF, Curcio CA. Visualizing retinal pigment epithelium phenotypes in the transition to geographic age-related macular degeneration. *Retina*. 2016;36:S12–S25.
51. Miller JW. Age-related macular degeneration revisited–piecing the puzzle: the LXIX Edward Jackson memorial lecture. *Am J Ophthalmol*. 2013;155:1–35.
52. Carido M, Zhu Y, Postel K, et al. Characterization of a mouse model with complete RPE loss and its use for RPE cell transplantation. *Invest Ophthalmol Vis Sci*. 2014;55:5431–5444.
53. Hanus J, Anderson C, Sarraf D, Ma J, Wang S. Retinal pigment epithelial cell necroptosis in response to sodium iodate. *Cell Death Discov*. 2016;2:1–9.
54. Kaneko H, Dridi S, Tarallo V, et al. DICER1 deficit induces Alu RNA toxicity in age-related macular degeneration. *Nature*. 2011;471:325–330.
55. Longbottom R, Fruttiger M, Douglas RH, Martinez-Barbera JP, Greenwood J, Moss SE. Genetic ablation of retinal pigment epithelial cells reveals the adaptive response of the epithelium and impact on photoreceptors. *Proc Natl Acad Sci U S A*. 2009;106:18728–18733.
56. Justilien V, Pang JJ, Renganathan K, et al. SOD2 knockdown mouse model of early AMD. *Invest Ophthalmol Vis Sci*. 2007;48:4407–4420.
57. Seo SJ, Krebs MP, Mao H, Jones K, Conners M, Lewin AS. Pathological consequences of long-term mitochondrial oxidative stress in the mouse retinal pigment epithelium. *Exp Eye Res*. 2012;101:60–71.
58. Mao H, Seo SJ, Biswal MR, et al. Mitochondrial oxidative stress in the retinal pigment epithelium leads to localized retinal degeneration. *Invest Ophthalmol Vis Sci*. 2014;55:4613–4627.
59. Feher J, Kovacs I, Artico M, Cavallotti C, Papale A, Balacco Gabrieli C. Mitochondrial alterations of retinal pigment epithelium in age-related macular degeneration. *Neurobiol Aging*. 2006;27:983–993.

Investigative Ophthalmology & Visual Science